Self-Consistent Simulation of Transport and Energy Deposition of Intense Laser-Accelerated Proton Beams in Solid-Density Matter

J. Kim,[1] B. Qiao,[1,*] C. McGuffey,[1] M. S. Wei,[2] P. E. Grabowski,[3] and F. N. Beg[1,†]
[1]Center for Energy Research, University of California, San Diego, California 92093, USA
[2]General Atomics, San Diego, California 92186, USA
[3]Department of Chemistry, University of California, Irvine, California 92697, USA
(Received 6 November 2014; published 28 July 2015)

The first self-consistent hybrid particle-in-cell (PIC) simulation of intense proton beam transport and energy deposition in solid-density matter is presented. Both the individual proton slowing-down and the collective beam-plasma interaction effects are taken into account with a new dynamic proton stopping power module that has been added to a hybrid PIC code. In this module, the target local stopping power can be updated at each time step based on its thermodynamic state. For intense proton beams, the reduction of target stopping power from the cold condition due to continuous proton heating eventually leads to broadening of the particle range and energy deposition far beyond the Bragg peak. For tightly focused beams, large magnetic field growth in collective interactions results in self-focusing of the beam and much stronger localized heating of the target.

DOI: 10.1103/PhysRevLett.115.054801 PACS numbers: 41.75.Ak, 41.75.Cn, 41.75.Jv

The study of intense ion beam dynamics in various conditions is a growing field of research as the beams are appealing for their potential applications in a broad range of nuclear research fields including high-yield neutron sources [1], exotic isotope creation [2,3], and the ion fast ignition inertial fusion concept [4,5]. They are widely used today as a high-fluence radiography source [6]. A leading method for producing intense ion beams utilizes short-pulse lasers to accelerate protons to high energy (>MeV) [7] in strong current beams (tens of kiloamperes) that can be focused to tens of micrometers [8], resulting in sufficiently high intensity (10^{10} A/cm^2) to achieve isochoric heating [9], enabling fundamental material studies including electron-ion equilibration [10] and equation of state [11,12] measurements. We show that complex, nonlinear behavior can emerge from these strongly dynamical systems, and an accurate understanding of the evolution of both the beam and target is crucial for all of these applications.

In cold materials (or low-density beams where the variation of target temperature is negligible), the stopping power of individual protons is well understood [13,14]. Calculations and measurements of proton energy deposition in specialized inertial confinement fusion targets (hot dense plasmas), where collisional drag dominates, have also been well documented [15–19]. However, due to the uniquely high intensity of a laser-accelerated proton beam, its interaction with solid-density matter is still not well understood because the thermodynamic state (charge, density, and temperature distributions) of the matter significantly changes, and collective beam behaviors become important.

With intense proton beams, solid-density matter can be rapidly heated to become partially ionized warm dense matter (WDM) [20], having density 0.1–10 times that of a solid and temperature 1–100 eV. In this regime, both bound and free electrons contribute to the proton stopping power, and their respective contributions change with the heated matter thermodynamic state. Therefore, to accurately calculate intense beam transport and energy deposition, both the matter's response to the beam (heating, ionization) and the beam's response to the matter (changes of density, charge, and stopping power) need to be taken into account simultaneously. Additionally, for an intense beam, collective interaction effects may substantially affect beam transport, including background return (neutralizing) currents, self-generated magnetic fields, filamentation instability, etc. These behaviors have been considered in a study of proton beam transport in tenuous plasmas [21] but not yet for solid targets.

In this Letter, we report for the first time the self-consistent hybrid particle-in-cell (PIC) simulation of transport and energy deposition of intense proton beams in solid-density (and/or warm dense) matter, where both the individual proton slowing-down and the collective beam-plasma interaction effects are taken into account in a dynamically coupled manner. To achieve this, a new proton stopping power module covering both cold solid-density and WDM regimes has been developed for the hybrid PIC code LSP [22]. In the module, at each simulation grid and time step, the proton stopping power is updated with the varying local target thermodynamic state (including charge, temperature, and density distributions) during beam transport. Impact ionization and heating capacity are loaded from the equations of state tables produced by PROPACEOS [23]. The PIC capability of LSP describes the collective effects in beam-matter interactions, providing a unique tool for self-consistently modeling intense beam transport.

The stopping power of a particle in matter is defined as its average energy loss per unit path length. As mentioned above, in the WDM regime, both bound and free electrons contribute. Therefore, the stopping power in LSP is calculated as [14–15,24]

$$(dE/dx)_{\text{total}} = (dE/dx)_{\text{bound}} + (dE/dx)_{\text{free}} = KN[(Z_2 - Z_{\text{eff}})f_{\text{bound}} + Z_{\text{eff}} f_{\text{free}}], \quad (1)$$

where N is the atomic density, Z_{eff} is the effective charge state, Z_2 is the target atomic number, f_{bound} and f_{free} represent the bound and free electron contribution functions, respectively. K is equal to $4\pi(Z_1 e^2)^2/\text{MeV}^2$, where Z_1 is the projectile particle atomic number ($Z_1 = 1$ for the proton) and Z_{eff} is determined from the equations of state. Note that the nuclear stopping power is negligible here. For example, the contribution of nuclear stopping felt by a 10 keV proton in a cold Al target is below 5% of its electronic stopping. For f_{bound}, we use the high-velocity Bethe-Bloch formula [13] with mean ionization potential and shell corrections using the experimental fitting method [25]. For f_{free}, both binary collisions and plasma oscillation excitations are considered using the homogeneous semiclassical Chandrasekhar approximation [15,19].

Figure 1(a) plots the calculated proton stopping power in solid aluminum as a function of proton energy for initial target temperatures of $T_e = T_i = 10$, 100, and 300 eV using the new implementation of LSP. When the target temperature rises, more free electrons contribute to stopping power while the number of bound electrons significantly drops. Since the free electron stopping power contribution generally has a peak value when the beam proton velocity is near the background electron thermal velocity in the target [26], the peak of the proton stopping power shifts to higher energy ranges when the target temperature increases. Correspondingly, the Bragg peak of the proton energy deposition curve obtained from the simulations using a single test particle with energy 2 MeV is flattened with increasing T_e, shown in Fig. 1(b).

In order to benchmark this new implementation, we compared our simulation with a recent quantum theoretical model (SCAALP) [26,27]. Figure 1(c) shows a comparison of the projected ranges (the maximum stopping depth) of protons in solid Al with initial energies of, respectively, 1, 3, and 5 MeV. The SCAALP model and the model implemented in LSP represent two different paradigms for modeling stopping power in partially ionized systems. In the SCAALP model, the total proton stopping power is calculated using the local-density and average-atom approximations, which take into account the inhomogeneous total electron density by using sophisticated homogeneous stopping power values locally in an assumed spherically symmetric confined ion. In our implemented module, described in detail above, we make different approximations in order to have a stopping power expression that can be evaluated quickly.

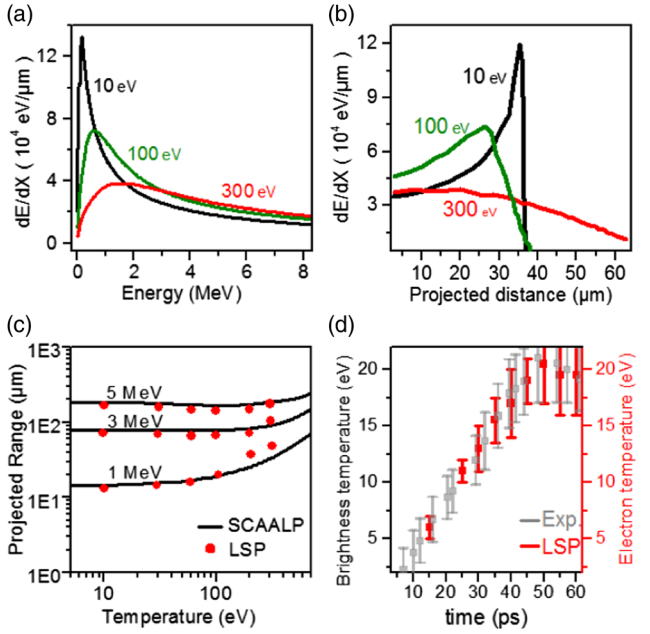

FIG. 1 (color online). (a) The calculated proton stopping power in LSP (with the new implementation) as a function of proton energy with target temperatures of $T_e = T_i = 10$, 100, and 300 eV, (b) the corresponding Bragg curves of 2 MeV protons, (c) comparisons of the proton projected ranges in solid Al from LSP simulations with those from the SCAALP theory [26,27], and (d) comparison of the temporal evolution of the heated target temperature from LSP simulation and experimental measurement [11].

As shown in Fig. 1(c), these approximations are expected to be most severe when the proton velocity is of the order of or less than the electron thermal velocity.

We also compared our simulation results with experimental data taken on the Titan laser [11], where a laser-driven proton beam was used to heat an aluminum solid target whose temperature was measured using streaked optical pyrometry. Figure 1(d) plots the temporal evolution of the temperature at near the critical density ($1–4 \times 10^{21}/\text{cm}^3$) of a heated solid Al target from simulations of an intense proton beam, where the beam has the average energy of 2 MeV (Maxwellian energy distribution characterizing the proton beam in the experiment), and a total energy of 5 J, which is about 5% of the laser energy. It appears to be consistent with the experimentally measured brightness temperature [11].

Several aspects of intense proton beam transport and energy deposition in solid-density matter warrant self-consistent modeling. Three issues are investigated: (i) dynamically varying the stopping power as a function of beam current density, (ii) collective effects of beam-plasma interactions, and (iii) transport of a realistic laser accelerated proton beam.

First, the effect of the dynamic changes of proton stopping power on beam transport and energy deposition is studied. Simulations were conducted in two-dimensional (2D) Cartesian (XZ) coordinates with the grid size 0.25 μm

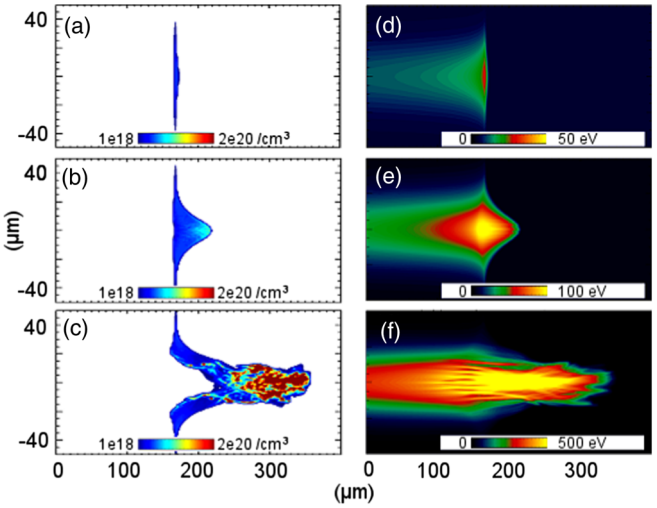

FIG. 2 (color online). LSP simulation results of proton beam transport in a solid Al target, showing proton beam density (left) and target temperature distributions (right), at time $t = 17$ ps. The beams have the same monoenergetic energies of 5 MeV, flattop distributed pulse durations 3 ps, and transversely Gaussian radii 14 μm, but different current densities of, respectively, (a), (d) 10^9, (b),(e) 10^{10}, and (c),(f) 10^{11} A/cm^2.

and the time interval 0.66 fs. Since the laser-accelerated proton beam is a quasineutral plasma jet [5], we inject both protons and comoving electrons with the same moving velocities. Corresponding to MeV protons, the comoving electrons have an energy of only several keV, which stop at distances <1 μm in solids. The effect of these comoving electrons plays a role only at a very early stage, and had no impact on proton transport here, unlike in Ref. [21].

Figure 2 plots the proton beam density and target temperature maps at time $t = 17$ ps when the proton beam has traversed and completely stopped in a solid Al target for different beam current densities of 10^9, 10^{10}, and 10^{11} A/cm^2. Other beam parameters are fixed, e.g., monoenergetic energies (5 MeV), flattop durations (3 ps), and Gaussian radii (14 μm). The initial target charge state is assumed to be 3+ and its temperature is 10 eV.

For low current density beams [Figs. 2(a) and 2(d)], the target is weakly heated to <30 eV, and the proton stopping power and projected range hardly change from that of a cold state. Longitudinally, all protons are stopped at nearly the same depth, leading to a localized heated region. This is consistent with the Bragg peak approximation for a single particle in a cold target. However, when the beam current density is increased to 10^{10} A/cm^2 [Figs. 2(b) and 2(e)], the inside of the target is heated to ~100 eV, where protons injected later (beam pulse tail) reach this area and experience reduced stopping power [see the stopping power for the energy range <0.5 MeV in Fig. 1(a)]. This eventually results in a deeper beam transport distance of ~210 μm and a nonlocalized energy deposition. When an intense beam of 10^{11} A/cm^2 [Figs. 2(c) and 2(f)] is used, this trend continues, showing a much deeper distance (>300 μm) and wider heated area. Additionally, beam transport and energy deposition also show obvious filamentation structures, which are rooted in the collective behaviors discussed below.

Second, collective beam-plasma interaction effects on transport and energy deposition are investigated. Here, similar simulations are run as described above with fixed beam current density 10^{10} A/cm^2 but the beam radius was chosen to be narrow ($r_0 = 7$ μm) or wide (14 μm). In order to show the importance of self-consistent modeling for this study, we carry out three categories of simulations by (i) switching off both the stopping power updating and the field updating modules (i.e., the stopping power is fixed at the 10 eV values and the self-field generation is excluded), (ii) switching the stopping power updating module on but the field updating module off, and (iii) switching on both self-consistent calculation modules.

Figures 3(a)–3(c) show the final heated target (ion) temperature maps, T_i, for all three cases. For case (i) [Fig. 3(a)], the heated target region is highly localized at the end of the proton projected depth, 175 μm. For case (ii), the stopping power decreases and the Bragg peak is flattened. Therefore, the beam experiences a dynamic and delocalized energy deposition, as shown in Fig. 3(b). Because of their having the same current density, both the narrow and wide beam cases show the same final heated target temperature maps [comparing Fig. 3(b) with Fig. 2(e)].

However, the final temperature maps of the narrow and wide beam cases are significantly different when a self-consistent simulation [case (iii)] is carried out, as shown in Figs. 3(c) and 3(d), respectively. For the narrow beam case, the heated region is confined to the central axis. The maximum temperature (~350 eV) is more than 3 times that of the wide case despite having the same current densities. This demonstrates that the collective interaction effect plays an important role in beam transport and energy deposition. The electric field generated by the proton beam drives the electron return current (neutralizing current) moving in the direction of beam propagation [28]. This return current causes self-generated resistive magnetic fields determined by $\partial B_y/\partial t = -\nabla \times (\eta J_{\mathrm{cold}})$, where η is the target resistivity and J_{cold} is the target return current, which has been well studied for electron beam transport [29–30]. This magnetic field B_y depends on the beam current density gradient $\partial J_z/\partial x$ and/or the resistivity gradient $\partial\eta/\partial x$ such that $-\partial B_y/\partial t = \eta(\partial J_z/\partial x) + (\partial\eta/\partial x)J_z$ in our simulation geometry, where η is determined by the local electron T_e and density. Because of its larger current density gradient, the narrow beam transport in the target can induce a stronger (>100 T) magnetic field [Fig. 3(g), in contrast with Fig. 3(h)], which focuses the beam protons, while background cold electrons experience a force directed radially outward. The field scales approximately linearly with current density gradient very soon

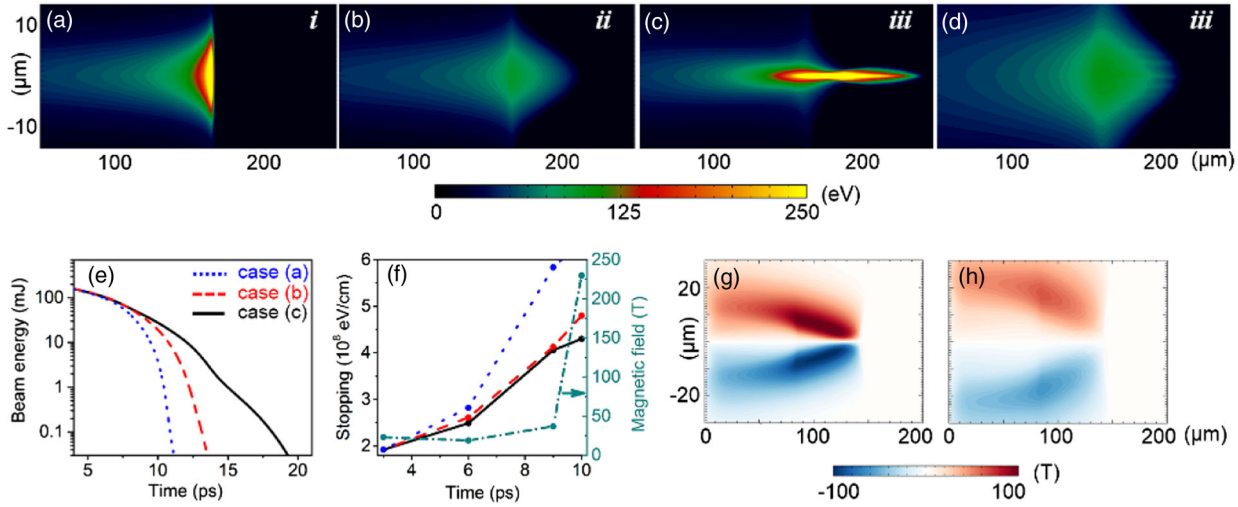

FIG. 3 (color online). Results of LSP simulations similar to Fig. 2, with beam current density 10^{10} A/cm^2 and a narrower beam radius $r_0 = 7$ μm, where the other parameters are the same. Panels (a)–(c) are the final heated target temperature maps at $t = 17$ ps for, respectively, the three categories (i)–(iii). Panel (d) corresponds to (c) but with the wide beam radius 14 μm case of Fig. 2. Panel (e) is the temporal evolutions of the total beam energy depositions, where dotted, dashed, and solid lines are for the cases (a), (b), and (c), respectively. Panel (f) is the corresponding evolution of the measured stopping power on axis and the evolution of the self-generated magnetic field at $r = r_0/4$ in (c). Panels (g) and (h) show the azimuthal magnetic fields generated in the simulations of (c) and (d), respectively.

after beam injection while heating remains weak but eventually depends on the varying target resistivity caused by the beam energy deposition.

Figure 3(e) plots the temporal evolution of the total beam energy deposition for each of the three cases, showing that by updating the stopping power and collective beam-plasma interactions, the energy deposition rate of the beam is reduced and its deposition depth increases. This has two causes: (i) the stopping power drops relative to the cold stopping rate with a rising target temperature [compare the dotted (blue) and dashed (red) lines in Fig. 3(f)] and (ii) the beam is focused by a self-generated magnetic field, leading to a further increase of the target temperature and a reduction of the stopping power [compare the dashed (red) and solid (black) line in Fig. 3(f)]. It should be noted that the additional dimension in 3D might bring about some differences from 2D, in particular upon the impact of the self-generated magnetic fields.

Lastly, we note that laser-accelerated proton beams generally have a broad, Maxwellian energy distribution of the form $dN/dE \sim \exp(-E/T_p)$. Furthermore, these beams can be focused by using spherically curved targets [9] that result in a smaller beam radius and higher current density compared to the divergent beam generated from planar targets. Figure 4 compares the simulation results of transport and energy deposition for a wide (current density 5×10^9 A/cm^2 and beam radius 44 μm) and a narrow (5×10^{10} A/cm^2 and 12 μm) proton beam in an Al target, with the total energy being 6 J in both cases. The protons are injected with only longitudinal momentum (neither diverging nor focusing) and a Maxwellian energy distribution having a mean energy of 4 MeV and a pulse duration of 5 ps for both beams.

For the wide beam, the most heated region of the target is near the beam injection plane within a depth <30 μm, and the maximum temperature is only 50 eV, shown in Figs. 4(a) and 4(b). This corresponds to the fact that a large number of particles have low energy and fewer have high

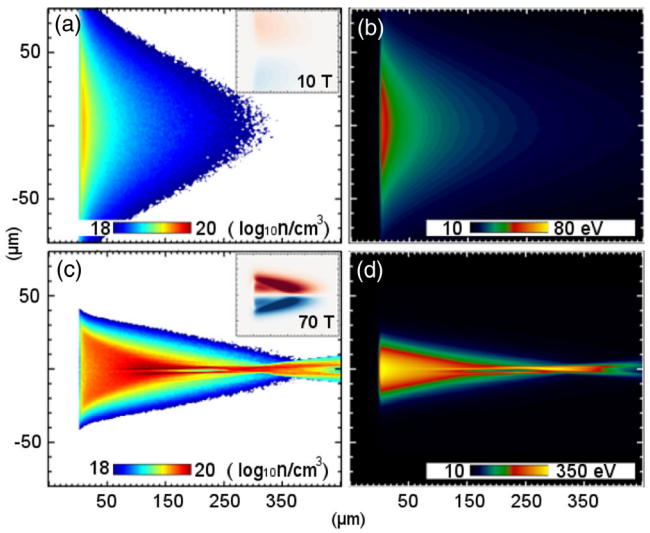

FIG. 4 (color online). Proton density (left) and heated target temperature (right) of Maxwellian proton beams in Al targets at $t = 20$ ps. Panels (a) and (b) are for a broad beam, having current density 5×10^9 A/cm^2 and a radius of 44 μm; (c) and (d) are for a narrow beam of 5×10^{10} A/cm^2 and 12 μm. Both beams have the same total energy of 6 J.

energy in a Maxwellian beam. However, once the beam is focused, as a result of the larger current density and stronger self-generated magnetic field from a small beam radius [inset of Fig. 4(c)], the beam can heat the target to a much higher temperature, above 350 eV, at deeper depths, ~300 μm [see Figs. 4(c) and 4(d)]. We conclude that a focused Maxwellian beam will more efficiently heat a target to a higher maximum temperature and a greater distance than a divergent beam because its deposition is localized, and it is more likely to self-pinch. This result clearly shows how collective effects and nonlinearities significantly affect beam energy deposition in size-sensitive applications.

In summary, we have for the first time self-consistently studied transport and energy deposition of intense laser-accelerated proton beams in evolving hybrid solid or warm dense matter states by PIC simulations. With the unique modeling capability, we have shown that both the individual proton slowing-down and the collective beam-plasma interaction effects play important roles in intense beam transport. It is also found that, given the same total beam energy, a focused proton beam can heat the target much deeper and to a higher maximum temperature. The results in this work reveal that collective effects must be considered in applications requiring high energy deposition in a tightly localized area such as ion/proton fast ignition (<40 μm) and nuclear physics (maximum fluence). Further, these results give guidelines for the onset of collective effects, which will impact a wide range of applications such as uniform volumetric heating in WDM studies. Current lasers are capable of delivering energies of >1 kJ, which could potentially produce proton beams with up to 100 J. By applying techniques of proton focusing to obtain intense beams these collective effects may be observable at existing facilities.

This work was supported by the U.S. DOE under Contracts No. DE-AC52-07NA27344 and No. DE-NA0002034 and by the U.S. AFOSR under Contract No. FA9550-14-1-0346.

*bqiao@ucsd.edu
†fbeg@ucsd.edu

[1] G. M. Petrov, D. P. Higginson, J. Davis, Tz. B. Petrova, J. M. McNaney, C. McGuffey, B. Qiao, and F. N. Beg, Phys. Plasmas **19**, 093106 (2012); D. P. Higginson *et al.*, Phys. Plasmas **18**, 100703 (2011); M. Roth *et al.*, Phys. Rev. Lett. **110**, 044802 (2013).
[2] D. Habs, P. G. Thirolf, M. Gross, K. Allinger, J. Bin, A. Henig, D. Kiefer, W. Ma, and J. Schreiber, Appl. Phys. B **103**, 471 (2011).
[3] F. Hannachi *et al.*, Plasma Phys. Controlled Fusion **49**, B79 (2007).
[4] M. Roth *et al.*, Phys. Rev. Lett. **86**, 436 (2001); J. C. Fernández, B. J. Albright, F. N. Beg, M. E. Foord, B. M. Hegelich, J. J. Honrubia, M. Roth, R. B. Stephens, and L. Yin, Nucl. Fusion **54**, 054006 (2014).
[5] B. Qiao, M. E. Foord, M. S. Wei, R. B. Stephens, M. H. Key, H. McLean, P. K. Patel, and F. N. Beg, Phys. Rev. E **87**, 013108 (2013).
[6] J. A. Cobble, R. P. Johnson, T. E. Cowan, N. Renard-Le Galloudec, and M. Allen, J. Appl. Phys. **92**, 1775 (2002).
[7] R. A. Snavely *et al.*, Phys. Rev. Lett. **85**, 2945 (2000); E. L. Clark *et al.*, *ibid.* **84**, 670 (2000).
[8] T. Bartal *et al.*, Nat. Phys. **8**, 139 (2012).
[9] P. K. Patel, A. J. Mackinnon, M. H. Key, T. E. Cowan, M. E. Foord, M. Allen, D. F. Price, H. Ruhl, P. T. Springer, and R. Stephens, Phys. Rev. Lett. **91**, 125004 (2003).
[10] T. G. White *et al.*, Phys. Rev. Lett. **112**, 145005 (2014).
[11] G. M. Dyer *et al.*, Phys. Rev. Lett. **101**, 015002 (2008); G. M. Dyer, Ph.D. Thesis, The University of Texas, 2007.
[12] A. Pelka *et al.*, Phys. Rev. Lett. **105**, 265701 (2010).
[13] J. Lindhard and M. Scharff, Mat. Fys. Medd. K. Dan. Vidensk. Selsk **27**, 15 (1953).
[14] J. F. Ziegler, J. Appl. Phys. **85**, 1249 (1999).
[15] T. A. Mehlhorn, J. Appl. Phys. **52**, 6522 (1981).
[16] C. Deutsch, Laser Part. Beams **2**, 449 (1984).
[17] T. Peter and J. Meyer-Ter-Vehn, Phys. Rev. A **43**, 1998 (1991).
[18] G. Zwicknagel, Laser Part. Beams **27**, 399 (2009).
[19] P. Wang, T. M. Mehlhorn, and J. J. MacFarlane, Phys. Plasmas **5**, 2977 (1998); S. Atzeni, M. Temporal, and J. J. Honrubia, Nucl. Fusion **42** (2002); D. S. Hey, Ph.D. thesis, The University of California, Davis, 2007.
[20] R. W. Lee *et al.*, Laser Part. Beams **20**, 527 (2002).
[21] H. Ruhl, T. Cowan, J. Dahlburg, P. Parks, and R. Stephens, Nucl. Fusion **44**, 438 (2004).
[22] D. R. Welch, D. V. Rose, M. E. Cuneo, R. B. Campbell, and T. A. Mehlhorn, Phys. Plasmas **13**, 063105 (2006).
[23] http://www.prism-cs.com/Software/PROPACEOS/PROPACEOS.htm.
[24] H. Bethe, Ann. Phys. (Berlin) **397**, 325 (1930); H. Bethe, Z. Phys. **76**, 293 (1932); F. Bloch, Ann. Phys. (Berlin) **408**, 285 (1933); F. Bloch, Z. Phys. **81**, 363 (1933).
[25] H. Bichsel, Phys. Rev. A **65**, 052709 (2002).
[26] G. Faussurier, C. Blancard, P. Cossé, and P. Renaudin, Phys. Plasmas **17**, 052707 (2010).
[27] M. Gauthier, C. Blancard, S. N. Chen, B. Siberchicot, M. Torrent, G. Faussurier, and J. Fuchs, High Energy Density Phys. **9**, 488 (2013).
[28] I. D. Kaganovich, E. A. Startsev, A. B. Sefkow, and R. C. Davidson, Phys. Plasmas **15**, 103108 (2008).
[29] J. R. Davies, Phys. Rev. E **68**, 056404 (2003).
[30] A. P. L. Robinson, M. H. Key, and M. Tabak, Phys. Rev. Lett. **108**, 125004 (2012).